Global NEST Journal, **28** (XX), pp 1-16
Available online: 21/07/2026

Red mud biochar as an efficient peroxymonosulfate activator for tetracycline degradation: Synergistic radical/non-radical mechanisms and process optimization for sustainable waste valorization

Wang Jing[1], Zhou Ruirui[2], Wang Longji[2], Guan Tongshuang[2], Li Zhe[1]* and Xiaohui Zhao[2]

[1]Henan Provincial Ecological Environment Technology Center, Zhengzhou 450004, China
[2]School of Civil Engineering and Architecture, Zhengzhou University of Aeronautics, Zhengzhou, 450046, China
[3]Zhengzhou Electric Power Technology College, Zhengzhou, 451400, China

*Correspondence e-mail: lzbb1989711@163.com

Abstract

To address tetracycline (TC) pollution in water, red mud biochar (RM BC) was synthesized from red mud and peanut shells via a one-step pyrolysis method and subsequently used to activate peroxymonosulfate (PMS) for TC degradation. The RM BC/PMS system achieved over 99% removal of TC (initial concentration: 20 mg/L) within 120 min. Characterization by SEM, XRD and XPS revealed that Fe_3O_4 nanoparticles were uniformly dispersed on the biochar surface, providing abundant active sites. Response surface methodology was employed to optimize the degradation conditions, identifying an RM BC dosage of 0.81 g/L, PMS concentration of 0.57 mM and pH 7.13 as optimal, under which the experimental removal efficiency reached 99.5%. Radical quenching tests and EPR analysis demonstrated that TC degradation proceeded through both radical ($SO_4^{\bullet-}$, •OH, and $O_2^{\bullet-}$; approximately 56% contribution) and non-radical ($^1O_2$; approximately 44% contribution) pathways, with both playing indispensable roles. In addition, the RM BC catalyst retained over 82% removal efficiency after five consecutive reuse cycles, with leached as (the only detected heavy metal) measuring 4.5 µg/L, approximately 11 times below the regulatory limit of 50 µg/L (GB 3838-2002), confirming its high stability and environmental safety. Previous studies primarily focused on single-mechanism degradation or adsorption. In contrast, this work systematically elucidated the synergistic radical/non-radical pathways, statistically optimized conditions via RSM, and validated the material's environmental safety, offering a sustainable waste-to-resource strategy for treating antibiotic-polluted water.

Keywords: Red mud biochar; Peroxymonosulfate (PMS); Tetracycline; Advanced oxidation; Radical/non-radical mechanism; Response surface methodology; Waste valorization.

Received: 25/01/2026,

Accepted: 01/07/2026,

Available online: 21/07/2026

Graphical abstract

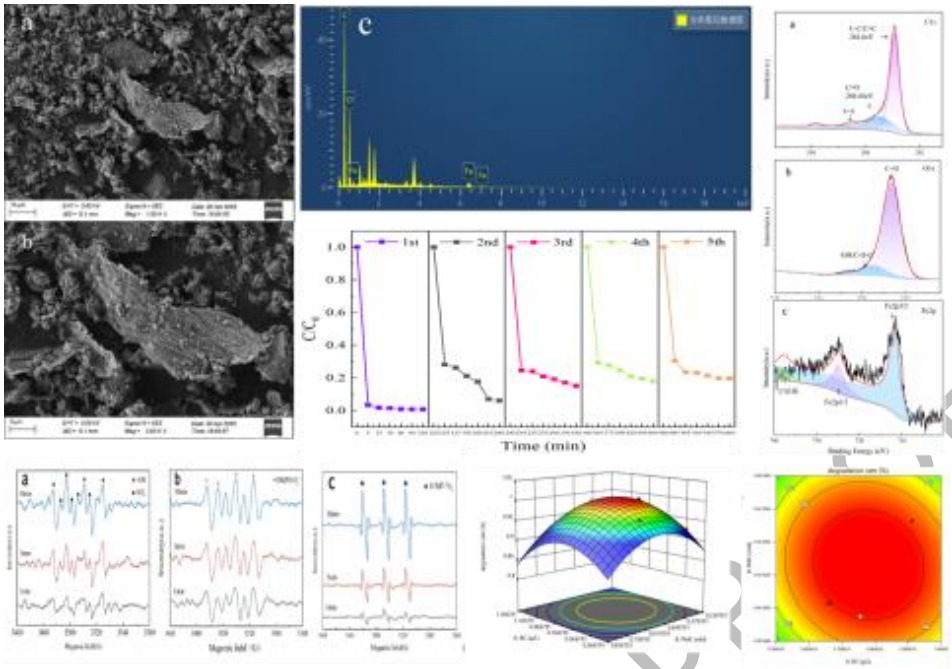

1. Introduction

Tetracycline (TC) was extensively used in livestock breeding, medical treatment, and aquaculture, leading to its persistent discharge into aquatic environments. Such release not only promoted microbial antibiotic resistance and disrupted ecological balance, but also posed potential risks to drinking water safety (Medha *et al.*, 2025, Sayed *et al.*, 2025, Sayed *et al.*, 2024a). Conventional wastewater treatment processes typically achieved only partial removal of antibiotics (50–70%), leaving biologically active residues that threatened receiving water bodies (Stapleton *et al.*, 2023).

Physical methods such as adsorption and membrane filtration effectively separated these pollutants, yet their practical application was often constrained by high operational costs and the generation of secondary waste streams requiring further disposal (Xu *et al.*, 2025, Sayed *et al.*, 2024b, Mohd Hanafiah *et al.*, 2024, Sayed *et al.*, 2024c). Chemical oxidation methods offered an alternative, but each presented intrinsic limitations: ozonation suffered from low utilization efficiency, potassium permanganate oxidation was highly sensitive to water quality parameters, and UV-based processes entailed substantial energy consumption (Xu *et al.*, 2025). Consequently, there was an urgent need to develop cost-effective and environmentally sustainable advanced oxidation technologies for emerging aquatic pollutants.

Persulfate-based advanced oxidation processes (SR-AOPs) emerged as promising alternatives for degrading persistent organic pollutants. Persulfate could be activated through various means, including thermal, microwave, ultrasonic, photochemical, electrochemical, and transition-metal-mediated methods (Pattnaik *et al.*, 2025, Çako *et al.*, 2024). Among these activation approaches, iron-based heterogeneous catalysis attracted particular attention owing to its operational simplicity, low energy requirements, and the low toxicity and environmental compatibility of iron (Li *et al.*, 2024). However, conventional iron-based catalysts often suffered from metal agglomeration, limited surface area, and insufficient stability under reaction conditions, which restricted their practical applicability.

To address these limitations, Fe_3O_4-rich biochar composites offered distinct advantages. The inverse spinel structure of magnetite (Fe_3O_4) contained both Fe^{2+} and Fe^{3+} in octahedral and tetrahedral sites, enabling efficient electron transfer during PMS activation through the Fe^{2+}/Fe^{3+} redox cycle without significant structural reorganization. Furthermore, the biochar matrix provided a porous carbonaceous support that not only dispersed the Fe_3O_4 nanoparticles and prevented agglomeration, but also contributed additional active sites through surface oxygen functional groups and defective carbon structures (Chen *et al.*, 2026, Yang *et al.*, 2026). This synergistic integration of Fe_3O_4 with biochar therefore held considerable promise for persulfate-based AOPs.

Red mud, an alkaline byproduct of alumina production containing over 10% iron, presented a compelling opportunity as a catalyst precursor (Albqmi *et al.*, 2025). Using iron-rich residues like red mud as catalyst precursors offered a practical substitute for commercial iron salts, eliminating the need for external iron sources and embodying the “waste-to-resource” principle (Gu *et al.*, 2024). Studies demonstrated that carbon materials derived from red mud performed well in various oxidation systems—including photocatalysis, ozonation, hydrogen

peroxide, and persulfate processes—for degrading organic pollutants (Cui *et al.*, 2024). However, the inherently limited pore structure of pristine red mud restricted its adsorption capacity and overall degradation efficiency toward antibiotics, and challenges related to long-term stability further constrained its practical applicability (Cao *et al.*, 2024).

Co-pyrolysis of red mud with lignocellulosic biomass was proposed as an effective strategy to overcome these limitations by enhancing porosity and introducing additional active sites (Zhang *et al.*, 2025). Peanut shells, an abundant agricultural residue rich in fiber, readily formed a porous carbon framework during pyrolysis (Zhang *et al.*, 2024). When co-pyrolyzed with red mud, the abundant surface functional groups on the resulting peanut shell biochar interacted synergistically with the components of the red mud (Qiu *et al.*, 2025). This synergistic interaction not only enhanced the porosity of the composite but also generated well-dispersed active sites that facilitated the catalytic degradation of antibiotics.

Despite the growing body of literature on red mud-based materials, several critical knowledge gaps remained. Most prior studies on red mud-biochar composites focused primarily on adsorption or single-mechanism degradation pathways, without systematically dissecting the relative contributions of radical versus non-radical species using combined quenching and EPR approaches (Wang *et al.*, 2025). Furthermore, previous work rarely employed statistical modeling tools such as response surface methodology (RSM) to simultaneously optimize multiple operational parameters and evaluate factor interactions. In addition, the interfacial regulation mechanisms governing the co-pyrolytic structural evolution and their relationship to catalytic performance had yet to be thoroughly examined. A comprehensive assessment integrating catalyst reusability, heavy metal leaching, and biotoxicity evaluation was also largely absent from earlier investigations. This study was therefore designed to fill these gaps by providing a systematic investigation that combined mechanistic elucidation, statistical optimization, and environmental safety validation within a single framework. Unlike previous studies that employed chemical modification or multi-step synthesis, our approach uses one-step co-pyrolysis without any chemical reagents, generating no secondary wastewater and offering a simpler, more sustainable preparation route.

To address these knowledge gaps, this study aimed to: (1) synthesize a novel RM-BC composite via one-step co-pyrolysis of red mud and peanut shell biomass; (2) systematically investigate the TC degradation performance and elucidate the underlying mechanisms, including both radical ($SO_4^{\bullet-}$ and •OH) and non-radical ($^1O_2$) pathways, with semi-quantitative estimation of their relative contributions; (3) employ response surface methodology (RSM) to optimize key operational parameters and evaluate factor interactions; and (4) evaluate catalyst reusability, broad-spectrum applicability, heavy metal leaching, and biotoxicity to comprehensively assess environmental safety. It was hypothesized that the co-pyrolysis process would generate a hierarchical porous structure with uniformly dispersed Fe_3O_4 active sites, enabling efficient PMS activation and synergistic radical/non-radical degradation. This work was expected to provide both a theoretical foundation and practical guidance for the high-value utilization of industrial and agricultural wastes in treating complex antibiotic pollution in water.

2. Materials and Methods

2.1. *Material Preparation*

The red mud used in this study was sourced from an aluminum production company in Sanmenxia, Henan Province, China. The raw red mud was first dried at 60 °C for 6 h to remove residual moisture, then ground and sieved through a 100-mesh screen. Peanut shells were obtained from Qi County, Kaifeng, Henan Province, China. They were washed three times with deionized water to remove surface dust and impurities, dried at 70 °C for 4 h, crushed into a fine powder using a mechanical grinder, and sieved through an 80-mesh screen. Both pretreated materials were stored in sealed containers at room temperature prior to use.

To determine the optimal mass ratio, a series of RM-BC composites were prepared at red mud-to-peanut shell (RM:BC) mass ratios of 0:1, 1:0, 1:1, 1:2, 1:3, 1:5, and 2:1 and subsequently evaluated for their PMS activation performance toward TC removal (TC concentration: 20 mg/L, volume: 50 mL). After 120 min of degradation, the TC removal efficiencies for the different ratios were as follows: 0:1 (78.50%), 1:0 (81.83%), 1:1 (82.93%), 1:2 (85.28%), 1:3 (90.86%), 1:5 (99.00%), and 2:1 (89.25%). The composite prepared at the 1:5 ratio exhibited the highest catalytic activity, which was attributed to an optimal balance between sufficient iron loading from red mud for effective PMS activation and adequate biomass-derived carbon for porosity development and active site dispersion. Consequently, the 1:5 ratio was adopted for all subsequent experiments (**Table 1**).

Table 1. The TC removal efficiencies for the different ratios.

Composites mass ratios (RM : BC)	0:1	1:0	1:1	1:2	1:3	1:5	2:1
TC removal (%)	78.50%	81.83%	82.93%	85.28%	90.86%	99.00%	89.25%

The pretreated red mud and peanut shell powders were thoroughly mixed at a mass ratio of 1:5 and divided into three equal portions. Each portion was placed in a quartz boat and transferred into a horizontal tube furnace. The mixture was heated to 700 °C at a ramp rate of 5 °C/min under a continuous high-purity N_2 atmosphere at a flow rate of 0.2 L/min. The temperature was held at 700 °C for 1 h, followed by an annealing treatment at the same

temperature for 2 h. Throughout the entire pyrolysis process—including the heating, holding, annealing, and natural cooling stages—the furnace was continuously purged with N_2 to maintain an oxygen-free environment. After the annealing period, the furnace was allowed to cool naturally to room temperature under the same continuous N_2 flow. The resulting red mud biochar (RM-BC) was collected, weighed, and stored in an airtight container for subsequent use. Based on the total mass of the precursors, the yield of RM-BC was in the range of approximately 35%–48%.

2.2. *Experimental Design*

For a typical degradation experiment, 50 mL of TC solution (20 mg/L) was added to a 150 mL conical flask, followed by the addition of RM-BC (0.75 g/L unless otherwise specified) and PMS (0.45 mM unless otherwise specified). The PMS used in this study was potassium peroxymonosulfate (analytical reagent grade) purchased from Shanghai Macklin Biochemical Technology Co., Ltd. (China). The reaction was conducted in a thermostatic shaker at 25 °C and 150 rpm for 120 min. RM-BC and PMS were added simultaneously without a pre-adsorption equilibrium step, as this procedure was designed to simulate practical wastewater treatment conditions where catalyst and oxidant are typically dosed together for operational efficiency. At predetermined time intervals, 1.5 mL aliquots were withdrawn, and "the reaction was immediately quenched by adding 0.1 mL of 1.0 M sodium thiosulfate ($Na_2S_2O_3$) solution, which rapidly consumed residual PMS and reactive radicals." The quenched sample was immediately filtered through a 0.45 µm syringe filter and analyzed for residual TC concentration by measuring absorbance at 355 nm using a UV–Vis spectrophotometer. TC concentrations were measured at predetermined time intervals according to previously reported procedures (Shi *et al.*, 2024, Hong *et al.*, 2026). A calibration curve was constructed using TC standard solutions at concentrations of 0.1, 0.5, 1, 2, 5, 10, and 20 mg/L, measured at 355 nm with a T9CS UV-Vis spectrophotometer (Beijing Puxi). The linear regression equation was y = 0.0290x + 0.0143 (R^2 = 0.9998), demonstrating excellent linearity. The method detection limit (MDL) was determined to be 0.05 mg/L based on 3 σ/slope, and the relative standard deviation (RSD) of triplicate measurements was consistently below 2%.

The solution pH was adjusted to the desired value using 0.1 mol/L HCl and 0.1 mol/L NaOH when investigating pH effects; for other experiments, the initial pH was maintained at 8.0. Three control experiments were performed in parallel: (i) TC solution with RM-BC alone (adsorption control, without PMS), (ii) TC solution with PMS alone (oxidation control, without catalyst), and (iii) TC solution only (blank control). All degradation experiments were conducted in triplicate, and the mean values ± standard deviation (SD) are reported.

Kinetic analysis was performed by fitting the TC degradation data to a pseudo-first-order model: $\ln(C_t/C_0) = -k_{obs}\, t$, where C_0 and C_t are the TC concentrations at time 0 and time t, respectively, and k_{obs} is the apparent rate constant. The k_{obs} values were determined from the slopes of the linear regression plots of $\ln(C_t/C_0)$ versus t.

The morphology and microstructure of the RM-BC samples were observed using Scanning Electron Microscopy equipped with Energy Dispersive X-ray Spectroscopy (SEM-EDS, Sigma 360, ZEISS, Germany). The crystal phases were identified by X-ray Diffraction (XRD, Aeris, PANalytical, Netherlands) with Cu Kα radiation over a 2θ range of 5°–90°. The surface elemental composition and chemical valence states were analyzed by X-ray Photoelectron Spectroscopy (XPS, K-Alpha, Thermo Scientific, USA).

To identify the dominant reactive species responsible for TC degradation, quenching experiments were carried out. Three radical scavengers were individually introduced into the RM-BC/PMS system under identical reaction conditions: methanol (MeOH, 1.0 M) as a scavenger for both $SO_4^{\bullet-}$ and •OH, tert-butanol (TBA, 1.0 M) for •OH, and L-histidine (L-His, 10 mM) for $^1O_2$. The quenching experiments were also performed in triplicate.

2.3. *Analysis method*

At predetermined time intervals, 1.5 mL of the reaction solution was withdrawn and immediately filtered through a 0.45 µm syringe filter into a 1.5 mL centrifuge tube. The absorbance of the filtrate was measured at 355 nm using a UV–Vis spectrophotometer (Hong *et al.*, 2026). All measurements were performed in triplicate. Error bars in all figures represent ± one SD of the triplicate measurements.

Statistical analysis was performed using SPSS software (version 26.0, IBM, USA). One-way analysis of variance (ANOVA) was conducted to evaluate the significance of differences among experimental groups, with statistical significance set at $p < 0.05$. Significant differences between treatment groups in the figures of Section 3.2 were indicated by different lowercase letters (e.g., a, b, c).

The TC removal efficiency (η, %) was calculated using the following equation:

$$\delta_E = (a*\delta_L - h\delta_A - \varepsilon)/(1 - h + \varepsilon_k)$$

η--The removal rate of the target pollutant, expressed as a percentage.

C_0--Initial concentration of tetracycline solution, mg/L

C_t--Concentration of tetracycline solution at equilibrium, mg/L

3. Results and Discussion

3.1. *Properties of Red Mud Biochar*

3.1.1. SEM analysis

The SEM images in **Figure 1(a) and (b)** displayed the morphology of RM-BC at different magnifications. **Figure 1(a)** (scale bar = 10 µm) showed the overall morphology of the material, while **Figure 1(b)** (scale bar = 5 µm) presented a higher-magnification view of the surface details. The material exhibited a flake-like structure with a rough surface, onto which numerous fine particles were densely attached. EDS analysis confirmed that these particles were

predominantly iron oxides derived from the red mud precursor. This uniform dispersion of Fe-rich phases was observed throughout the carbon matrix, suggesting that the co-pyrolysis process effectively integrated the iron oxides within the biochar support. Elemental mapping (**Figure 1(c)–(e)**) further revealed the co-distribution of Fe and C throughout the material, with Fe exhibiting a relatively even spatial dispersion. Such microscale integration of iron oxides within the carbon framework has been reported to facilitate synergistic catalytic effects between the carbonaceous support and the metal active centers (Chen *et al.*, 2026).

It should be noted that while BET specific surface area and pore structure characterization were not included in the present study, the porous nature of biochar derived from lignocellulosic biomass under similar pyrolysis conditions is well established in the literature. Previous studies have reported that biochar prepared from peanut shells and comparable agricultural residues via pyrolysis at 600–800 °C typically possesses high specific surface areas (200–500 m^2/g) with well-developed micro- and mesoporous structures (Zhang *et al.*, 2024, Qiu *et al.*, 2025, Chen *et al.*, 2026). These documented findings provide supporting evidence for the porosity-related discussion in the present work.

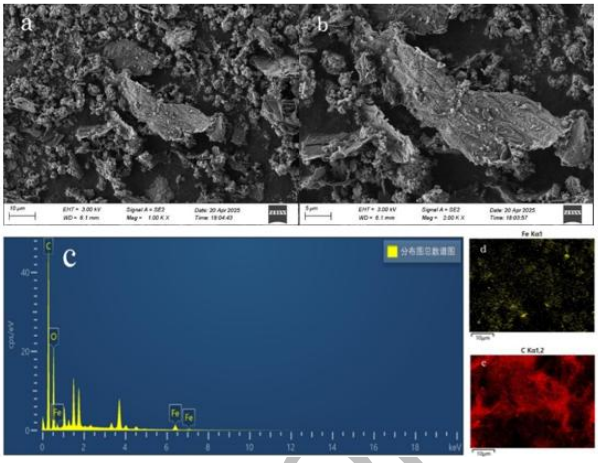

Figure 1. SEM images of RM-BC at (a) low and (b) high magnification; elemental mapping of (c) C, (d) Fe, and (e) merged image.

3.1.2. FTIR Analysis of Material Functional Groups

The FTIR spectrum of the RM-BC composite was presented in **Figure 2**. A broad absorption band centered at 3443.3 cm^{-1} corresponded to O–H stretching vibrations, indicating abundant surface hydroxyl groups. These –OH groups served as critical anchoring sites for PMS molecules, facilitating the formation of surface complexes (≡M–OH–HSO_5^-) that initiated electron transfer and PMS activation (Liu *et al.*, 2025).

The peaks at 1438.3 cm^{-1} and 695.0 cm^{-1} were assigned to C=C and C–H stretching modes, respectively, confirming the formation of an aromatic carbon framework during pyrolysis (Jian *et al.*, 2025). The aromatic C=C structures contributed to PMS activation by acting as electron donors and providing π-electron-rich regions that facilitated non-radical electron transfer pathways from the pollutant to PMS (Xu *et al.*, 2023a).

The signal observed at 993.3 cm^{-1} was attributed to C–O–C (ether) or C–O (alcohol/phenol) stretching vibrations, rather than C=O stretching as initially assigned. Carbonyl (C=O) stretching vibrations typically appear at higher wavenumbers (1700–1750 cm^{-1}), and the absorption band at approximately 1000 cm^{-1} is more consistently assigned to C–O–C or C–O groups in biochar-based materials (Jian *et al.*, 2025, Xu *et al.*, 2023a). These oxygen-containing functional groups may have participated in PMS activation by facilitating the generation of $^1O_2$ through non-radical pathways, as surface-bound C–O–C/C–O groups have been reported to promote the decomposition of PMS to singlet oxygen (Zhang *et al.*, 2024).

The characteristic peak at 470.1 cm^{-1} was attributed to Fe–O vibrations. The presence of Fe–O bonds confirmed the successful incorporation of iron oxide species from the red mud into the biochar matrix, which was consistent with the SEM-EDX and XRD results. The Fe–O moieties served as the primary active centers for PMS activation, where the Fe^{2+}/Fe^{3+} redox cycle generated $SO_4^{\bullet-}$ and •OH radicals. Furthermore, the proximity of Fe–O sites to the carbonaceous functional groups (–OH, C=C, C–O–C) on the biochar surface may have promoted synergistic interactions, where the carbon matrix facilitated electron transfer to the iron centers, enhancing the overall catalytic efficiency (Liu *et al.*, 2025, Chen *et al.*, 2026).

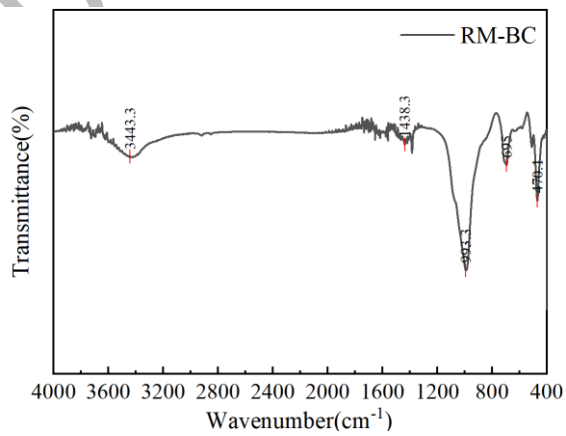

Figure 2. FT-IR spectra of RM-BC.

3.1.3. XRD

Figure 3 presented the XRD pattern of RM-BC. The diffraction peaks observed at 2θ = 21.2°, 35.2°, 41.6°, 51.1°, 68.0°, and 74.1° were indexed to the (111), (220), (311), (400), (511), and (440) crystal planes of magnetite (Fe_3O_4, JCPDS No. 88-0866), respectively (Li *et al.*, 2022). Fe_3O_4 was identified as the primary crystalline iron phase in the RM-BC composite, as no diffraction peaks corresponding to other iron oxides (e.g., α- Fe_2O_3 or γ- Fe_2O_3) were detected. The XPS analysis (Section 3.1.4) provided complementary evidence for the coexistence of Fe^{2+} and Fe^{3+}, which was consistent with the Fe_3O_4 assignment.

The selective formation of Fe_3O_4 under the co-pyrolysis conditions was consistent with the carbothermal reduction mechanism reported in the literature. During co-pyrolysis, the lignocellulosic components of peanut shells decomposed to generate reducing gases (e.g., CO, H_2) and carbonaceous species, which facilitated the reduction of

iron oxides (primarily hematite, α- Fe_2O_3) present in the raw red mud to magnetite (Fe_3O_4) (Zhang *et al.*, 2025, Qiu *et al.*, 2025, Gu *et al.*, 2024).

The inverse spinel structure of magnetite, which contained both Fe^{2+} and Fe^{3+} in octahedral and tetrahedral sites, was structurally advantageous for PMS activation, as it enabled efficient electron transfer through the Fe^{2+}/Fe^{3+} redox cycle without significant structural reorganization. The absence of other crystalline iron oxide phases in the XRD pattern suggested that the co-pyrolysis conditions employed in this study favored the selective formation of magnetite, which has been reported to exhibit superior catalytic activity compared to other iron oxides in persulfate-based AOPs (Li *et al.*, 2022).

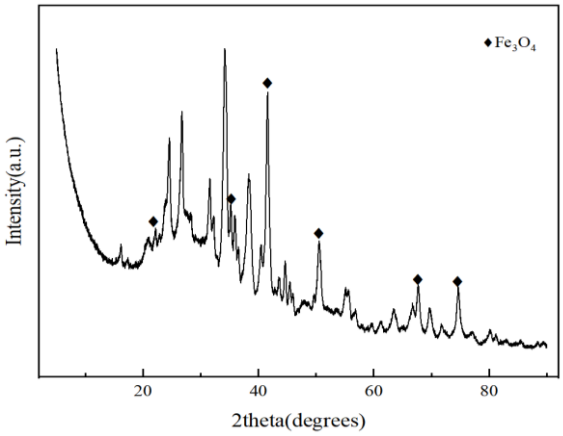

Figure 3. XRD pattern of RM-BC.

3.1.4. XPS

The surface chemical composition and elemental valence states of RM-BC were further investigated by XPS. The survey spectrum (**Figure 4**) confirmed the presence of C, O, and Fe as the major surface constituents. The high-resolution C 1s spectrum (**Figure 5(a)**) could be deconvoluted into three peaks at 284.8 eV, 286.1 eV, and 288.5 eV, corresponding to C–C/C=C, C–O, and O–C=O functional groups, respectively (Xu *et al.*, 2023a). These oxygen-containing functional groups on the biochar surface served dual roles: they provided adsorption sites for PMS molecules and participated in electron transfer processes during catalysis. The O 1s spectrum (**Figure 5(b)**) exhibited peaks at 530.1 eV, 531.8 eV, and 533.2 eV, which were assigned to lattice oxygen in metal oxides (Fe–O), surface hydroxyl groups (–OH), and adsorbed water, respectively (Xu *et al.*, 2023a). The abundant surface hydroxyl groups were consistent with the O–H stretching vibrations observed in the FTIR spectrum (**Figure 2**).

The Fe 2p spectrum (**Figure 5(c)**) displayed characteristic peaks at 711.9 eV and 724.9 eV, corresponding to Fe $2p_{3/2}$ and Fe $2p_{1/2}$, respectively. Deconvolution of the Fe $2p_{3/2}$ peak confirmed the coexistence of Fe^{2+} (710.8 eV) and Fe^{3+} (713.5 eV) on the catalyst surface (Zhao *et al.*, 2019). The presence of both Fe oxidation states was consistent with the Fe_3O_4 phase identified by XRD, where Fe^{2+} and Fe^{3+} occupy the octahedral and tetrahedral sites of the inverse spinel structure. This Fe^{2+}/ Fe^{3+} coexistence was mechanistically essential, as it enabled the continuous redox cycle: Fe^{2+} sites activated PMS to generate $SO_4^{\bullet-}$ radicals, while the resulting Fe^{3+} was regenerated back to Fe^{2+} through reaction with PMS or electron transfer from the biochar matrix, thereby sustaining the catalytic degradation of TC (Chen *et al.*, 2026, Yang *et al.*, 2026).

The XPS results further supported the existence of electron transfer interactions between the carbon matrix and iron species. The C–O and O–C=O groups identified in the C 1s spectrum, together with the aromatic C=C framework (284.8 eV), could serve as electron donors, facilitating the reduction of Fe^{3+} to Fe^{2+} on the catalyst surface. This electron transfer pathway was thermodynamically favorable and contributed to the regeneration of active Fe^{2+} sites, maintaining efficient PMS activation. Furthermore, the graphitized carbon structure, as evidenced by the prominent C–C/C=C peak, may have provided conductive pathways for electron shuttling from the carbon framework to the iron centers. Such synergistic interactions between the carbonaceous support and Fe_3O_4 nanoparticles enhanced the overall catalytic efficiency and contributed to the sustained degradation of TC observed in the RM-BC/PMS system (Xu *et al.*, 2023a, Zhao *et al.*, 2019).

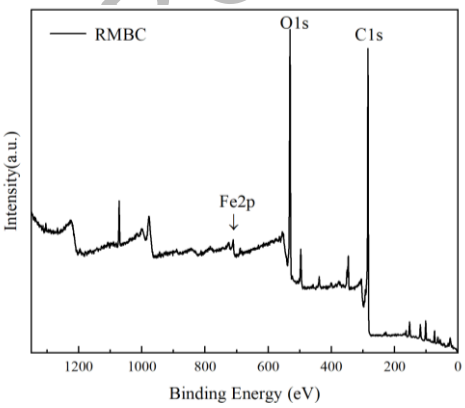

Figure 4. XPS full spectrum of RM-BC.

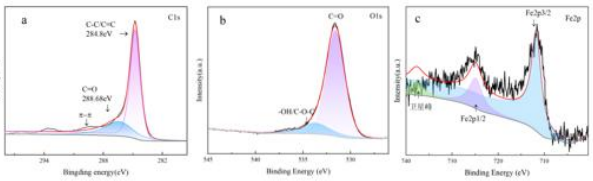

Figure 5. High-resolution XPS spectra of RM-BC: (a) C 1s, (b) O 1s, and (c) Fe 2p.

3.2. *Catalytic Degradation Performance*

3.2.1. RM-BC removal efficiency under different systems

The TC removal performance was compared across three different systems: RM-BC adsorption alone, PMS oxidation alone, and the combined RM-BC/PMS system. As shown in **Figure 6**, RM-BC adsorption alone achieved a TC removal of 87.12% within 120 min, indicating that the composite possessed a substantial adsorption capacity attributable to its developed pore structure and abundant surface functional groups. However, it should be noted that adsorption merely transferred TC from the aqueous phase to the solid phase without destroying the pollutant molecule, posing a potential risk of desorption and secondary pollution under changing environmental conditions.

PMS oxidation without catalyst achieved only 70.57% removal, confirming the limited oxidative capacity of PMS in the absence of an activator and highlighting the necessity of catalytic activation.In contrast, the RM-BC/PMS system removed 99.1% of TC within the same period, significantly outperforming both individual treatments. The marked enhancement from 87.12% (adsorption alone) to 99.1% (RM-BC/PMS) demonstrated that catalytic degradation contributed substantially beyond physical adsorption. The reactive species generated via PMS activation (Section 3.3.1) degraded the adsorbed TC and regenerated surface active sites, enabling a synergistic adsorption–degradation mechanism (Zeng *et al.*, 2025).

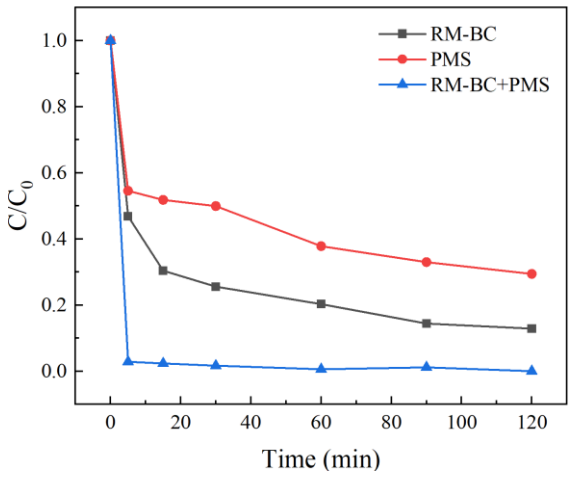

Figure 6. Removal rate of TC under different systems.

3.2.2. Effect of RM-BC Dosage on TC Removal

The effect of RM-BC dosage on TC removal was shown in **Figure 7**. As the RM-BC dosage increased from 0.25 g/L to 0.75 g/L, the TC removal rate rose markedly from 65.3% to 99.1%, and the corresponding apparent rate constant (k_{obs}) increased from 0.0084 min^{-1} to 0.0326 min^{-1}. The concurrent enhancement in both removal efficiency and kinetic rate was attributed to the increased number of active sites available for PMS activation and TC adsorption. However, when the dosage was further increased to 1.0 g/L, the removal rate exhibited only a marginal gain to 99.5%, and k_{obs} increased only slightly to 0.0341 min^{-1}, indicating a kinetic plateau. This plateau could be attributed to two factors: (i) the saturation of active sites, as excessive catalyst dosage caused uneven PMS dispersion and reduced the effective utilization of individual active sites; and (ii) the self-quenching reaction of sulfate radicals ($SO_4^{\bullet-} + SO_4^{\bullet-} \rightarrow S_2O_8^{2-}$), which consumed reactive radicals and diminished the incremental benefit (Fu *et al.*, 2024). Considering both removal efficiency and cost-effectiveness, a dosage of 0.75 g/L was identified as optimal.

3.2.3. Effect of PMS dosage on TC removal

The influence of PMS concentration on TC removal was presented in **Figure 8**. Increasing the PMS concentration from 0.35 mM to 0.45 mM enhanced the removal efficiency by 6.49%, with k_{obs} rising from 0.0243 min^{-1} to 0.0326 min^{-1}. However, a further increase to 0.60 mM yielded only an additional 0.35% improvement, and k_{obs} increased only marginally to 0.0338 min^{-1}. This marginal gain was attributed to the saturation of active sites on the catalyst surface: when the available active sites approached full occupancy, excess PMS could not be effectively activated and remained in solution without participating in the degradation reaction (Shen *et al.*, 2025)."

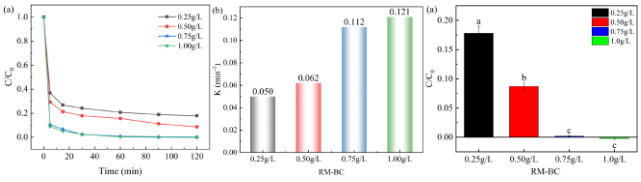

Figure 7. Effect of RM-BC dosage on TC removal.

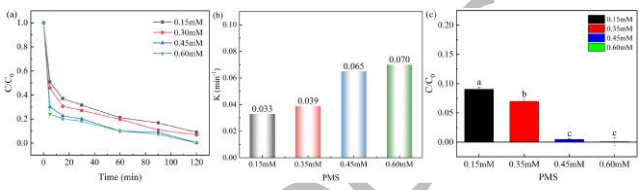

Figure 8. Effect of different PMS dosage on TC removal.

3.2.4. Effect of Initial pH on TC Removal

As shown in **Figure 9**, the TC removal rates at pH 8 and pH 10 reached 99.13% (k_{obs} = 0.0326 min^{-1}) and 95.97% (k_{obs} = 0.0281 min^{-1}), respectively, both significantly higher than those at pH 4 (89.30%, k_{obs} = 0.0172 min^{-1}) and pH 6 (90.97%, k_{obs} = 0.0185 min^{-1}).

The improved performance under alkaline conditions was explained by several synergistic mechanisms. First, surface-bound activation was enhanced: hydroxylated metal oxide sites (≡M–OH) on the RM-BC surface formed complexes with PMS, promoting direct electron transfer to TC. Previous studies on iron-based biochar composites have reported that surface hydroxyl groups exhibit optimal PMS binding affinity under neutral to weakly alkaline conditions, where the catalyst surface carries a moderate charge density conducive to PMS adsorption and activation (Xiao *et al.*, 2025). Second, alkaline pH favored the generation of $^1O_2$ via PMS self-decomposition and reactions with surface defect sites (Zhang *et al.*, 2024). Third, the pH-dependent speciation of TC also contributed to the observed trend. At pH > 9, TC existed predominantly as anions (TC^-), which could be electrostatically attracted to localized positive charges on metal oxide surfaces, even when the overall biochar surface was negatively charged. This localized electrostatic enrichment concentrated TC near catalytic active sites, enhancing degradation efficiency (Xu *et al.*, 2023a). Under acidic conditions (pH 4), the catalyst surface was extensively protonated, inhibiting PMS complexation with surface hydroxyl groups, and TC existed primarily as neutral molecules, which weakened the electrostatic interaction with the catalyst surface and resulted in a significantly lower degradation rate.

3.2.5. Effects of inorganic interfering ions and humic acid on TC removal

The effects of common coexisting substances--SO_4^{2-}, Cl^-, HCO_3^-, and humic acid (HA)--were evaluated and are shown in **Figure 10**. HA exhibited the most pronounced inhibition: the removal efficiency decreased from 87.41% (k_{obs} = 0.0211 min^{-1}) at 10 mg/L to 54.94% (k_{obs} = 0.0093 min^{-1}) at

20 mg/L, due to radical scavenging and competitive adsorption on active sites.

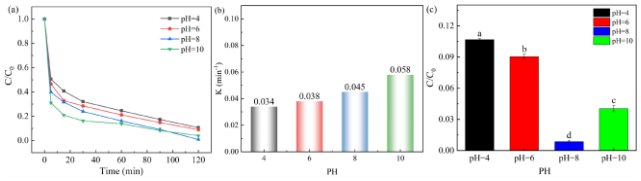

Figure 9. Effect of different pH on TC removal.

Among the inorganic anions, SO_4^{2-} exerted only a slight inhibitory effect (~2% reduction in removal efficiency, with a small decrease in k_{obs}), attributable to competitive occupation of active sites without directly participating in radical consumption reactions."

In contrast, Cl^- and HCO_3^- significantly suppressed TC removal, which could be attributed to their reactions with $SO_4^{\bullet-}$ and •OH to generate less reactive secondary species. Specifically, Cl^- reacted with $SO_4^{\bullet-}$ and •OH to form chlorine radicals (Cl•) and dichloride radical anions ($Cl_2^{\bullet-}$) (Equations 1–3):"

$$SO_4^{\bullet-} + Cl^- \rightarrow SO_4^{2-} + Cl\bullet \quad (1)$$

$$Cl\bullet + Cl^- \rightarrow Cl_2^{\bullet-} \quad (2)$$

$$\bullet OH + Cl^- \rightarrow OH^- + Cl\bullet \quad (3)$$

"Meanwhile, HCO_3^- scavenged $SO_4^{\bullet-}$ and •OH to generate carbonate radicals ($CO_3^{\bullet-}$) with lower oxidation capacity (Equations 4–5):"

$$SO_4^{\bullet-} + HCO_3^- \rightarrow SO_4^{2-} + CO_3^{\bullet-} + H^+ \quad (4)$$

$$\bullet OH + HCO_3^- \rightarrow CO_3^{\bullet-} + H_2O \quad (5)$$

"The resulting secondary species (Cl•, $Cl_2^{\bullet-}$, and $CO_3^{\bullet-}$) possessed lower oxidation potentials than $SO_4^{\bullet-}$ and •OH, thereby substantially reducing the TC degradation rate (Gu *et al.*, 2025, Li *et al.*, 2024)."

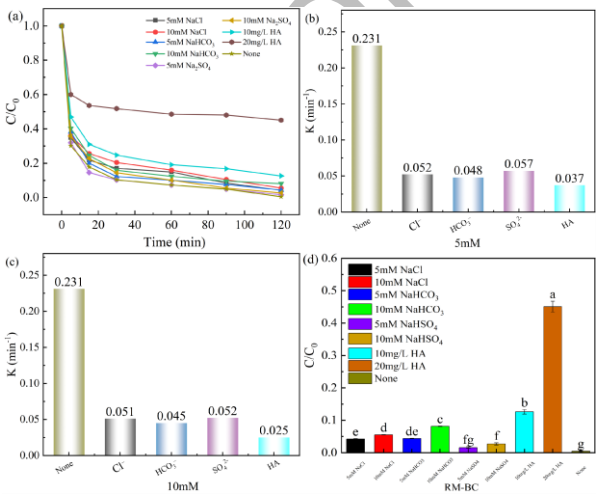

Figure 10. Effect of different interfering ions on TC removal.

3.2.6. Effect of Reaction Temperature on RM-BC Removal Efficiency

The temperature dependence of TC removal in the RM-BC/PMS system was shown in **Figure 11**. The removal rate increased from 96.5% (k_{obs} = 0.0261 min^{-1}) at 15 °C to 98.4% (k_{obs} = 0.0339 min^{-1}) at 30 °C. Higher temperatures accelerated PMS decomposition, increased the collision frequency between radicals ($SO_4^{\bullet-}$/•OH) and TC, and provided more energy to overcome the activation energy barrier. Moreover, warming enhanced non-radical pathways, particularly direct electron transfer at defective sp^2-carbon sites, thereby boosting $^1O_2$ generation. Across the entire tested range (15-30 °C), removal consistently exceeded 90%, demonstrating the system's robust adaptability to ambient temperature variations. The progressive increase in k_{obs} with temperature confirmed the thermally activated nature of the degradation process. Balancing removal efficiency and energy cost, 25 °C (room temperature) was identified as a practical optimum (Xu *et al.*, 2023b). Although the observed temperature dependence confirmed the thermally activated nature of the degradation process, the narrow temperature range (15-35 °C) and limited data points precluded reliable calculation of the apparent activation energy (Ea) via Arrhenius fitting.

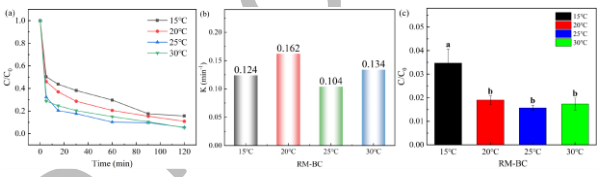

Figure 11. Effect of different reaction temperatures on TC removal.

3.3. *Mechanism analysis*

3.3.1. Identification of reactive oxygen species and their contributions

The reactive oxygen species (ROS) generated in the RM-BC/PMS system were qualitatively identified using electron paramagnetic resonance (EPR) spectroscopy, and their relative participations in TC degradation were assessed through selective chemical quenching experiments combined with kinetic analysis. For EPR characterization, DMPO (5,5-dimethyl-1-pyrroline N-oxide) was employed as the spin trap to capture radical species including •OH, $SO_4^{\bullet-}$, and $O_2^{\bullet-}$, while TEMP (2,2,6,6-tetramethylpiperidine) was used to trap the non-radical singlet oxygen $^1O_2$ (Gao *et al.*, 2022). As shown in **Figure 12(a)**, a characteristic 1:2:2:1 four-line EPR signal assigned to the DMPO-•OH adduct was clearly detected, accompanied by weak satellite peaks corresponding to the DMPO-$SO_4^{\bullet-}$ adduct, which directly verified the simultaneous generation of hydroxyl and sulfate radicals upon PMS activation (Cui *et al.*, 2025). **Figure 12(b)** exhibited a typical six-line sextet signal originating from DMPO-$O_2^{\bullet-}$, confirming the production of superoxide radical anions. In **Figure 12(c)**, a distinct 1:1:1 triplet signal assigned to the TEMP-$^1O_2$ adduct unambiguously validated the formation of singlet oxygen (Yang *et al.*, 2023, Ben Hamou *et al.*, 2025). All EPR spectra were re-plotted with explicit peak labels and signal assignments to improve readability. Collectively, the EPR spectroscopic evidence confirmed the coexistence of multiple radical ROS ($SO_4^{\bullet-}$, •OH, and $O_2^{\bullet-}$) and non-radical $^1O_2$ within the RM-BC/PMS catalytic system.

To evaluate the relative contributions of these ROS to TC degradation, quenching experiments were performed

using selective scavengers: methanol (MeOH) to scavenge both $SO_4^{\bullet-}$ and •OH, tert-butanol (TBA) to selectively quench •OH, sodium carbonate (Na_2CO_3) to capture $O_2^{\bullet-}$, and L-histidine (L-His) to quench $^1O_2$ (Thi Mai *et al.*, 2025). Na_2CO_3 was employed as an $O_2^{\bullet-}$ probe based on the following rationale: carbonate anions react with $SO_4^{\bullet-}$ and •OH to generate carbonate radicals ($CO_3^{\bullet-}$), which possess substantially lower oxidation potential and exhibit negligible reactivity toward TC. Therefore, the inhibition observed upon Na_2CO_3 addition was predominantly attributed to the elimination of $O_2^{\bullet-}$ rather than the consumption of primary radicals (Zeng *et al.*, 2025)."

The results of the quenching experiments were presented in **Figure 13**. "To provide a quantitative estimation of the relative contributions of individual ROS, the apparent rate constants (k_{obs}) obtained from pseudo-first-order kinetic fitting under each quenching condition were analyzed using the following equations (Yang *et al.*, 2026):"

$$fO_2^{\bullet-},TC = \frac{K_{obs} - K_{NaCO_3}}{K_{obs}} \times 100\% \quad (6)$$

$$fO^{\bullet}OH,TC = \frac{K_{obs} - K_{TBA}}{K_{obs}} \times 100\% \quad (7)$$

$$f^1O_2,TC = \frac{K_{MeOH} - K_{L-his}}{K_{obs}} \times 100\% \quad (8)$$

$$fSO_4^{\bullet-},TC = \frac{K_{TBA} - K_{MeOH}}{K_{obs}} \times 100\% \quad (9)$$

where k_{obs} represented the apparent rate constant without any scavenger, and $k_{scavenger}$ represented the apparent rate constant in the presence of the respective scavenger.

Based on these calculations, the estimated contributions of $SO_4^{\bullet-}$, •OH, $O_2^{\bullet-}$, and $^1O_2$ to TC degradation were approximately 3.04%, 70.43%, 89.56%, and 22.17%, respectively. These results identified •OH and $O_2^{\bullet-}$ as the primary reactive species responsible for TC degradation in the RM-BC/PMS system, while $SO_4^{\bullet-}$ and $^1O_2$ played secondary but non-negligible roles.

It must be emphasized that these contribution percentages were semi-quantitative estimates and should not be overinterpreted as absolute quantitative contributions. High-concentration quenching reagents may introduce confounding effects, including altering PMS decomposition kinetics, competing for surface active sites on RM-BC, and triggering cross-reactions between scavengers and non-target ROS species, which can lead to systematic bias in the estimation of individual ROS contributions (Zeng *et al.*, 2025, Dai *et al.*, 2025). These estimates were therefore intended to reflect the relative importance of each pathway rather than to provide precise absolute quantification.

Integrating the direct EPR spectroscopic evidence and the quenching experimental results, it was concluded that TC degradation in the RM-BC/PMS system proceeded through synergistic radical and non-radical dual pathways. The Fe^{2+}/Fe^{3+} redox cycle on the RM-BC surface triggered continuous PMS decomposition to generate diverse ROS. Both radical oxidation (primarily •OH and $O_2^{\bullet-}$, with minor participation of $SO_4^{\bullet-}$) and non-radical oxidation ($^1O_2$) worked cooperatively to achieve nearly complete TC removal (99.13%). A comprehensive catalytic mechanism schematic diagram was provided in **Figure 14**, systematically illustrating the PMS activation pathways on RM-BC, the Fe^{2+}/Fe^{3+} redox cycle, the multi-type ROS generation processes, and the TC degradation and mineralization pathways (**Table 2**).

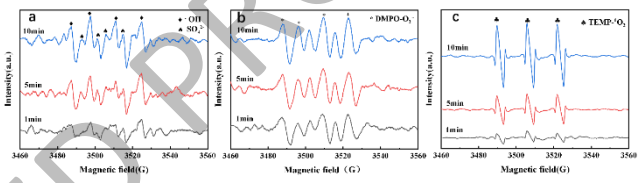

Figure 12. EPR spectra of the RM-BC/PMS system: (a) DMPO-•OH and DMPO- $SO_4^{\bullet-}$ adducts; (b) DMPO- $O_2^{\bullet-}$ adduct; (c) TEMP-$^1O_2$ adduct.

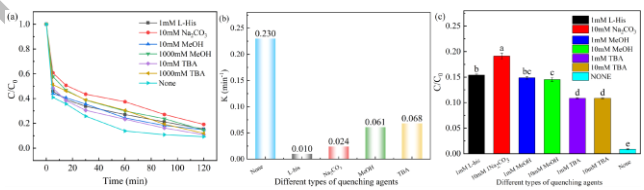

Figure 13. Free radical identification experiments.

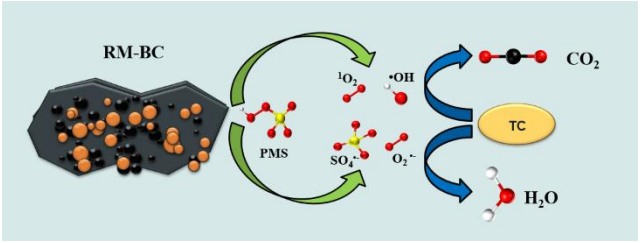

Figure 14. Ccatalytic mechanism diagram.

Table 2. Effects of different scavengers on TC removal in the RM-BC/PMS system.

Scavenger	Target species	Removal rate (%)	Inhibition (Δη, %)
None (control)	-	99.13	-
MeOH	$SO_4^{\bullet-}$ + •OH	85.11	14.02
TBA	•OH	89.13	10.00
Na_2CO_3	$O_2^{\bullet-}$	80.86	18.27
L-His	$^1O_2$	84.59	14.54

4. Practical Application Potential

4.1. *Stability and wide applicability*

4.1.1. Loop experiment

Under fixed reaction conditions (RM-BC: 0.75 g/L, PMS: 0.45 mM, pH = 8), five consecutive catalytic cycles were performed. After each cycle, the RM-BC catalyst was recovered by vacuum filtration, thoroughly washed with

deionized water and ethanol, and then dried at 60 °C for 12 h before reuse.

As shown in **Figure 15**, the composite maintained TC removal rates of 99.13% and 93.84% in the first and second cycles, respectively, demonstrating good catalytic stability. The removal efficiency decreased to 84.94% in the third cycle and further to 82.34% in the fifth cycle. Although this was lower than the initial use, the fifth-cycle removal efficiency remained comparable to the adsorption capacity of fresh RM-BC alone (87.12%, Section 3.2.1), indicating that the catalytic functionality was largely preserved even after repeated use.

FTIR analysis of RM-BC before and after the reaction (**Figure 15**) revealed notable changes in surface functional groups. The weakened -OH peak at approximately 3420 cm^{-1} indicated consumption of surface hydroxyl groups during the reaction. The enhanced C=O peak at approximately 1630 cm^{-1} suggested accumulation of oxidized intermediates on the catalyst surface. These changes indicated that the gradual decline in catalytic activity was primarily attributed to the blockage of active sites by adsorbed intermediates and the progressive consumption of surface functional groups involved in PMS activation (Feng *et al.*, 2016, Chen *et al.*, 2024).

These results demonstrated that RM-BC possessed satisfactory reusability, retaining substantial catalytic activity even after five consecutive cycles. This robust stability highlighted the potential of the composite to reduce treatment costs and minimize secondary pollution in practical applications.

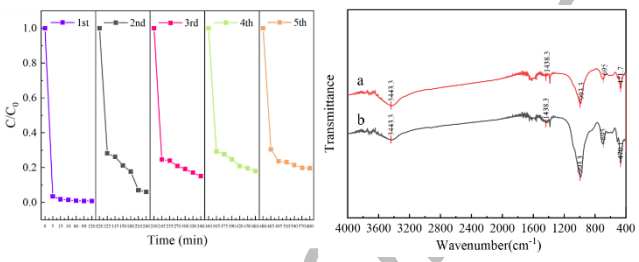

Figure 15. Removal effect of reusing a material of five times, FTIR spectra of the as-prepared catalyst before reaction (a) and after five consecutive reuse cycles (b).

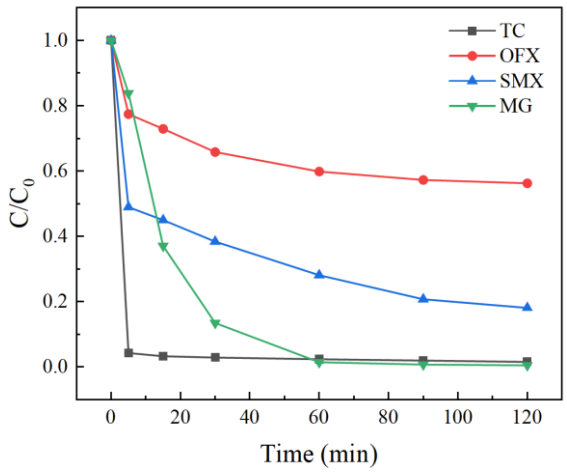

Figure 16. Proficiency testing experiment of RM-BC/PMS reaction system.

4.1.2. Broad-spectrum degradation performance

To evaluate the broad-spectrum applicability of the RM-BC/PMS system, the degradation of three additional organic pollutants-ofloxacin (OFX), sulfamethoxazole (SMX), and malachite green (MG)-was investigated under the same reaction conditions." As shown in **Figure 16**, the RM-BC/PMS reaction system achieved a removal rate of 43.74% for OFX, 81.92% for SMX, and 99.81% for MG within 120 min. "The distinct degradation efficiencies among different pollutants could be attributed to their molecular structural differences. TC and MG, which contain multiple hydroxyl groups and conjugated aromatic systems, exhibited strong surface complexation with Fe_3O_4 active sites on RM-BC, facilitating efficient catalytic degradation. OFX, bearing electron-withdrawing fluorine atoms on its quinolone backbone, possessed reduced electron density and was less susceptible to electrophilic attack by reactive oxygen species. SMX, with its sulfonamide group, showed intermediate reactivity. These results demonstrated that the RM-BC/PMS system possessed acceptable broad-spectrum degradation capability, although the efficiency varied depending on the molecular structure of the target pollutant (Qin *et al.*, 2025).

4.1.3. Material Safety

During the recycling of biochar, metal leaching may occur due to structural damage or exposure to oxidizing conditions, posing potential risks to aquatic ecosystems (Shen *et al.*, 2025). Therefore, the concentrations of heavy metals in the wastewater after five consecutive reuse cycles were determined. Nine elements of potential concern-Cr, Co, Ni, As, Cd, Pb, Mn, Mo, and Fe-were selected for analysis. As was measured by atomic fluorescence spectrometry according to HJ 694-2014, while the other metals were determined by inductively coupled plasma optical emission spectrometry (ICP-OES) according to HJ 776-2015. The results are presented in **Table 3**.

Among the nine tested metals, only as was detected, at a concentration of 4.5 µg/L, which is approximately 11 times lower than the Category III limit of 50 µg/L specified in the Surface Water Environmental Quality Standard (GB 3838-2002). All other metals were below their respective detection limits and well within the regulatory thresholds. Specifically, Cr was not detected (detection limit: 0.03 mg/L vs. limit: 0.05 mg/L), Co was not detected (< 0.02 mg/L vs. limit: 1.0 mg/L), Ni was not detected (< 0.007 mg/L vs. limit: 0.02 mg/L), Cd was not detected (< 0.05 mg/L vs. limit: 0.005 mg/L), Pb was not detected (< 0.1 mg/L vs. limit: 0.05 mg/L), Mn was not detected (< 0.01 mg/L vs. limit: 0.1 mg/L), Mo was not detected (< 0.05 mg/L vs. limit: 0.07 mg/L), and Fe was not detected (< 0.01 mg/L vs. limit: 0.3 mg/L).

It should be noted that the heavy metal leaching test was conducted under the neutral to weakly alkaline pH conditions (pH ~8) that were representative of the degradation experiments. In practical wastewater treatment, raw wastewater is typically neutralized in an equalization tank prior to advanced oxidation, meaning that the RM-BC catalyst would primarily encounter near-

neutral water. The negligible metal leaching observed under these conditions therefore reflected the anticipated performance in real treatment applications. Leaching behavior under extreme acidic conditions, which may be relevant for specific industrial effluents, warrants investigation in future studies.

These results demonstrated that the leaching of heavy metals from RM-BC after repeated use was negligible and posed no significant risk to receiving water bodies, confirming the material's environmental safety for practical applications (Chen *et al.*, 2024). In practical wastewater treatment engineering, raw wastewater typically undergoes flow equalization and pH neutralization in an equalization tank before advanced oxidation, ensuring that the influent to the oxidation unit is maintained at near-neutral pH. Therefore, evaluating heavy metal leaching under neutral to weakly alkaline conditions is practically relevant, as it reflects the actual operating conditions that the RM-BC catalyst would encounter in a real treatment train.

Table 3. Detection of Heavy Metals in Wastewater over Five Cycles.

Test Items	Test Results	Unit	Detection limit	Category III Limit for Surface Water Quality Standards[1]
Cr	ND	mg/L	0.03 mg/L	0.05 mg/L
Co	ND	mg/L	0.02 mg/L	1.0 mg/L
Ni	ND	mg/L	0.007 mg/L	0.02 mg/L
As	4.5	μg/L	0.3 μg/L	50 μg/L
Cd	ND	mg/L	0.05 mg/L	0.005 mg/L
Pb	ND	mg/L	0.1 mg/L	0.05 mg/L
Mn	ND	mg/L	0.01 mg/L	0.1 mg/L
Mo	ND	mg/L	0.05 mg/L	0.07 mg/L
Fe	ND	mg/L	0.01 mg/L	0.3 mg/L

[1] Category III limits from Surface Water Environmental Quality Standard (GB 3838-2002).

Table 4. Response Surface Analysis Scheme and Experimental Results

Experiment number	Influencing Factor A: Amount of catalyst added (g/L)	Influencing Factor B: PMS Concentration (mM)	Influencing Factor C: pH Value of the Initial Solution	Removal Rate (%)
1	0.75	0.30	10	96.23
2	0.50	0.45	6	96.00
3	0.50	0.45	10	96.20
4	0.75	0.60	6	99.59
5	0.50	0.60	8	96.74
6	1.00	0.30	8	96.68
7	0.50	0.30	8	92.67
8	0.75	0.30	6	95.91
9	0.75	0.60	10	99.67
10	1.00	0.60	8	99.71
11	1.00	0.45	6	99.54
12	0.75	0.45	8	99.76
13	0.75	0.45	8	99.80
14	0.75	0.45	8	100.00
15	0.75	0.45	8	100.00
16	1.00	0.45	10	99.79
17	0.75	0.45	8	99.94

Note: Run 15 originally recorded as 100.21% was corrected to 100.00%, as removal efficiency cannot physically exceed 100%.

4.1.4. Biotoxicity Testing

The biotoxicity of the treated TC solution was evaluated using mung bean germination and growth assays. Prior to the experiment, mung bean seeds were soaked in deionized water overnight to pre-screen germination viability. The selected seeds were then divided into three groups (20 seeds per group) and separately cultured in tap water (control), 20 mg/L TC solution (untreated), and the TC solution degraded by the RM-BC/PMS system (treated). The seeds were incubated at 25 ± 1 °C under a 12 h light/12 h dark photoperiod with a light intensity of 2000 lux. After 6 days of cultivation, the germination rate reached 100% in all three groups, indicating that neither TC nor its degradation intermediates inhibited seed germination under the tested conditions.

However, substantial differences were observed in seedling growth parameters (**Figure 18**). The root length in the treated group (3.09 ± 1.8 cm) was comparable to that of the control group (2.38 ± 1.1 cm), whereas the untreated group exhibited severely inhibited root elongation (0.55 ± 0.3 cm), corresponding to only 23.1% of the control. Similarly, the stem length in the treated group (13.91 ± 2.1 cm) closely matched the control (14.88 ± 2.3 cm), while the untreated group showed marked suppression (3.81 ± 0.5

cm, 25.6% of the control). Leaf length followed the same trend: the treated group (2.48 ± 0.6 cm) was nearly identical to the control (2.45 ± 0.5 cm), whereas the untreated group exhibited significantly reduced leaf growth (1.63 ± 0.5 cm). Statistical analysis was performed using one-way ANOVA in SPSS software. Significant differences (p < 0.05) among treatment groups were indicated by different lowercase letters in **Figure 18**.

These quantitative results demonstrated that the RM-BC/PMS treatment effectively eliminated the phytotoxicity of TC, restoring seedling growth to levels statistically indistinguishable from the control (Tian *et al.*, 2025). However, it should be noted that the degradation intermediates were not identified in the present study. While the recovery of seedling growth suggested a substantial reduction in phytotoxicity, the absence of intermediate identification meant that complete detoxification could not be fully confirmed. Certain intermediates may exhibit chronic toxicity or specific ecotoxicological effects not captured by the mung bean assay. Future studies should incorporate liquid chromatography-mass spectrometry (LC-MS) for intermediate identification and employ a battery of ecotoxicity tests to comprehensively assess the environmental safety of the treated effluent.

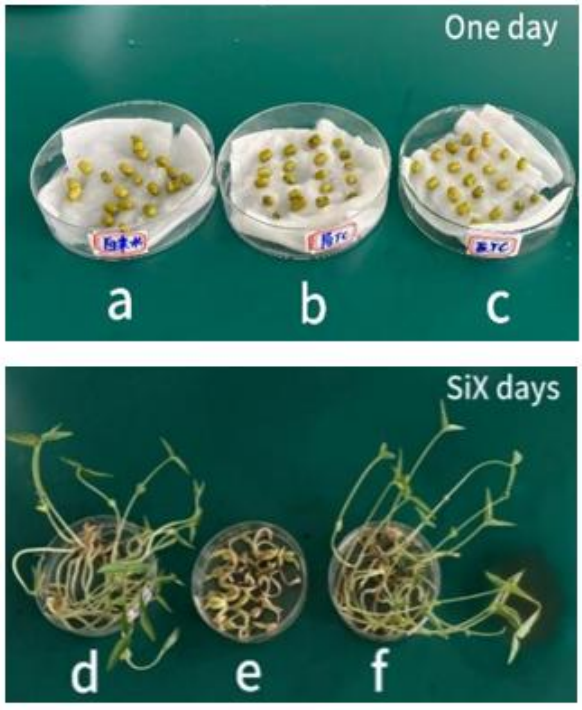

Figure 17. Photographs of mung bean germination and growth after 6 days in (a, d) tap water (control), (b, e) 20 mg/L TC solution (untreated), and (c, f) degraded TC solution (treated).

4.2. *Optimization of removal process parameters*

4.2.1. Establishment of the Box-Behnken Response Surface Model

The process parameters for TC removal in the RM-BC/PMS system were optimized using the Box-Behnken design (BBD) method in Design-Expert 13 software. Three independent variables were selected: RM-BC dosage (A, g/L), PMS concentration (B, mM), and initial solution pH (C). The initial TC concentration was fixed at 20 mg/L. The experimental design matrix and corresponding removal efficiencies are presented in **Table 4**.

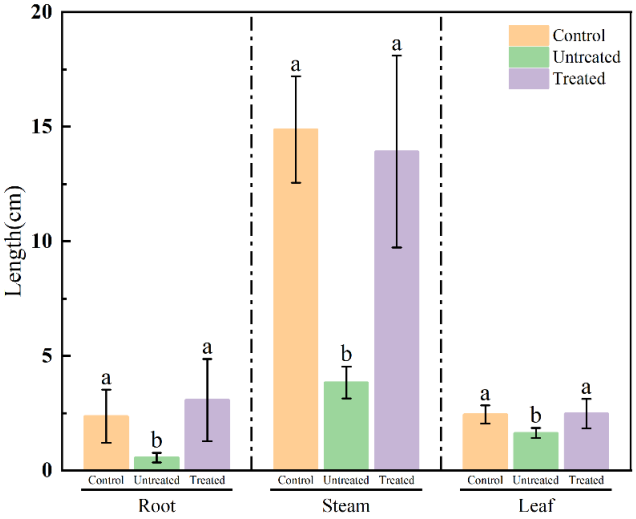

Figure 18. Comparison of root and leaf growth of mung bean seedlings after 6 days of cultivation in the three groups. Different lowercase letters above bars indicate statistically significant differences (p < 0.05, one-way ANOVA)

Based on multiple regression analysis of the experimental data, a quadratic polynomial model was constructed to describe the TC removal efficiency (Y, %) as a function of the coded variables:

$$Y = 0.9994 + 0.01763*A + 0.01776*B + 0.00106*C - 0.00259*AB + 0.00015*AC - 0.00060*BC - 0.01731*A2 - 0.01761*B2 - 0.00329*C2$$

where A, B, and C were the coded variables for RM-BC dosage, PMS concentration, and initial pH, respectively. The interaction coefficient AB was negative and significant, indicating an inhibitory effect of excessive catalyst and PMS combinations on removal efficiency. The AC and BC interaction coefficients were not significant (p > 0.05).

4.2.2. Analysis of Variance for the Response Surface Model

The statistical significance of the model was evaluated using analysis of variance (ANOVA), as summarized in **Table 5.** The model F-value of 469.36 (p < 0.0001) confirmed that the regression model was highly significant. The coefficient of determination (R^2 = 0.9983) and adjusted R^2 (R_{Adj}^2 = 0.9962) indicated an excellent fit, with the model explaining 99.83% of the total variability. The lack-of-fit was not significant (p = 0.9904), further validating the model adequacy.

The Adequate Precision (AP) value was 69.63, which was substantially greater than the minimum threshold of 4, confirming an excellent signal-to-noise ratio. The Coefficient of Variation (C.V.) was 0.1391%, indicating high precision and reproducibility of the experimental data.

Based on the F-values, the relative influence of the factors followed the order: PMS concentration (B) > RM-BC dosage (A) > initial pH (C). All quadratic terms (A^2, B^2, C^2) and the AB interaction were significant (p < 0.05), while “AC and BC interactions, as well as the linear effect of pH (C), were not statistically significant.”

Table 5. ANOVA results for the quadratic regression model.

Source of variance	Sum of squares	Degree of freedom	Mean Square	F-value	p-value
Regression model	0.0079	9	0.0009	469.36	< 0.0001
A – RM-BC dosage	0.0025	1	0.0025	1333.64	< 0.0001
B-PMS dosage	0.0025	1	0.0025	1354.42	< 0.0001
C-pH	8.92×10^{-6}	1	8.92×10^{-6}	4.79	0.0649
AB	2.96×10^{-5}	1	2.96×10^{-5}	14.45	0.0067
AC	9.53×10^{-8}	1	9.53×10^{-8}	0.051	0.8275
BC	1.43×10^{-6}	1	1.43×10^{-6}	0.77	0.4098
A^2	0.0013	1	0.0013	677.18	< 0.0001
B^2	0.0013	1	0.0013	700.33	< 0.0001
C^2	4.55×10^{-5}	1	4.55×10^{-5}	24.41	0.0017
Residual	1.30×10^{-5}0.0000	7	1.86×10^{-6}		
Lack of Fit	3.23×10^{-7}	3	1.08×10^{-7}	0.034	0.9904
Pure error	1.27×10^{-5}	4	$3.181.30\times10^{-6}$		
Total error	0.0079	16			

R^2=0.9983; R^2_{Adj}=0.9962; Adequate Precision = 69.63; C.V. = 0.1391%

Note: P<0.01 indicates a highly significant difference, and P<0.05 indicates a significant difference.

4.2.3. Response Surface Graph Analysis

(1) Combined effect of RM-BC dosage and PMS concentration

The combined effect of RM-BC dosage and PMS concentration at pH 8 was illustrated in **Figure 19**. "The approximately circular contour lines in **Figure 18(b)** indicated a relatively weak interaction between these two factors, although the AB term was statistically significant (*p* = 0.0067)." The removal efficiency exceeded 99% when the RM-BC dosage ranged from 0.66 to 1.0 g/L and the PMS concentration ranged from 0.42 to 0.62 mM. At excessively high PMS concentrations, a slight decline in removal efficiency was observed, which was attributed to the radical self-quenching effect, consistent with the single-factor experimental results (Section 3.2.2).

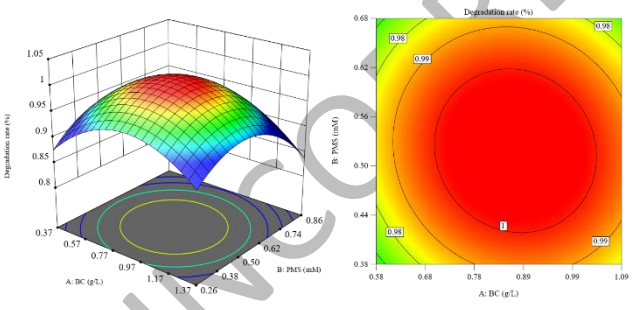

Figure 19. Interaction between biochar dosage and PMS dosage (a) 3D response surface plot; (b) contour plot

(2) Combined effect of RM-BC dosage and initial solution pH

At a fixed PMS concentration of 0.45 mM, the effects of RM-BC dosage and pH on TC removal were shown in **Figure 20**. The AC interaction was not statistically significant (*p* = 0.8275), and the nearly parallel contour lines in **Figure 19(b)** confirmed that no significant interaction existed between these two factors. Optimal removal was achieved at pH 6.15-10.5 and an RM-BC dosage of 0.75-1.0 g/L. This broad pH adaptability was consistent with the pH effect results (Section 3.2.4) and indicated that both radical and non-radical pathways remained effective across a wide pH range.

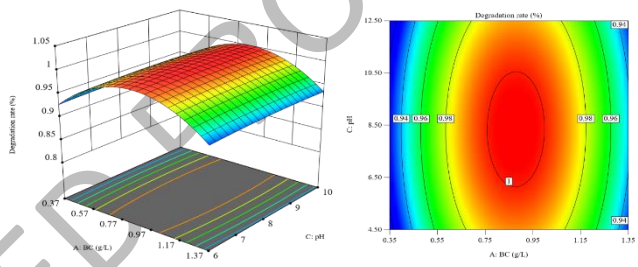

Figure 20. The interaction between the dosage of RM-BC and the initial pH of the solution (a) 3D response surface plot; (b) contour plot

(3) Combined effect of PMS dosage and initial solution pH

When the RM-BC dosage was fixed at 0.75 g/L, the combined effect of PMS concentration and initial pH was shown in **Figure 21**. The BC interaction was not statistically significant (*p* = 0.4098), and the contour lines in **Figure 20(b)** showed limited curvature, confirming the lack of significant interaction. Within the pH range of 6.02-10.42, the highest removal efficiency was observed when the PMS concentration was 0.48-0.60 mM, which was attributed to enhanced PMS decomposition in alkaline environments to generate reactive sulfate radicals.

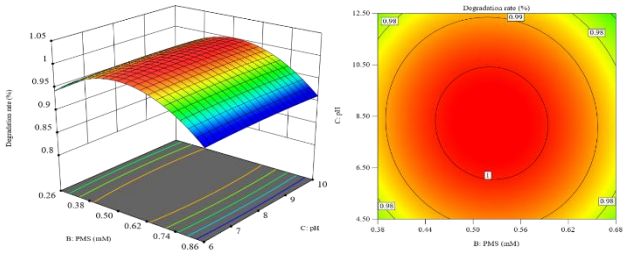

Figure 21. Interaction between the dosage of PMS and the initial pH of the solution (a) 3D response surface plot; (b) contour plot

4.2.4. Optimization of Removal Process Parameters

Based on the regression model prediction, the optimal reaction parameters were determined as: RM-BC dosage of 0.81 g/L, PMS concentration of 0.57 mM, and initial pH of 7.13. Under these optimized conditions, the predicted TC removal efficiency was 100.00%. It should be noted that

the model-predicted value of 100.00% represented the mathematical upper bound of the quadratic regression fitting at the theoretical optimum point, rather than a claim of absolute complete removal. In practice, near-complete removal is achievable, and the experimentally validated mean of 99.51% confirmed the model's reliability. Three independent confirmatory experiments were conducted under the optimized conditions. The experimental removal efficiencies were 99.47%, 99.33%, and 99.69% (mean = 99.51%), as shown in **Table 6**. The relative deviation between the experimental mean and the predicted value was less than 5%, confirming the reliability and predictive accuracy of the RSM model (Liu *et al.*, 2024).

Table 6 Experimental Validation Results of Reaction Parameters

Response (Y)	Predicted value	Exp. 1	Exp. 2	Exp. 3	Mean experimental value
Removal rate (%)	100.00	99.47	99.33	99.69	99.51

5. Conclusion

This study presented a sustainable waste-to-resource strategy by converting red mud and peanut shells into an efficient biochar catalyst (RM-BC) for peroxymonosulfate (PMS) activation, integrating mechanistic elucidation, statistical optimization, and environmental safety assessment within a single framework.Under optimized conditions (RM-BC: 0.81 g/L, PMS: 0.57 mM, pH: 7.13) identified by RSM, the RM-BC/PMS system achieved 99.51% TC removal within 120 min. EPR and quenching experiments combined with kinetic analysis confirmed that TC degradation proceeded through synergistic radical and non-radical pathways, with •OH and $O_2^{\bullet-}$ identified as the primary reactive species. The catalyst retained over 82% removal efficiency after five cycles with minimal heavy metal leaching, and the biotoxicity assay confirmed that the treated effluent supported normal plant growth. These results demonstrated that the RM-BC/PMS system held promising potential for treating antibiotic-polluted water, although validation using real wastewater matrices and continuous-flow conditions remained necessary. Future studies should also focus on identifying degradation intermediates and conducting comprehensive ecotoxicity assessments.

Acknowledgements

This work was supported by Key Research and Development Projects in Henan Province(241111320500), Henan Provincial Science and Technology Research Project (252102320129, 262102521031), the Scientific Research Team Plan of Zhengzhou University of Aeronautics (23ZHTD01012) and Provincial Innovation and Entrepreneurship and Training Program for College Students (202610485068). This study was also supported by Zhengzhou Key Laboratory of Watershed Environmental Treatment and Zhengzhou Key Laboratory of Environmental Functional Materials.

Data availability statement

All data that support the findings of this study are included within the article (and any supplementary files).

Conflicts of Interest

The authors declare that they have no conflicts of interest.

References

Albqmi, M., Belaiba, A. & Hodaifa, G. (2025) 'Red mud-efficient catalyst for the treatment of real olive mill wastewater through advanced oxidation toward greener and sustainable practices', *Journal of Water Process Engineering,* 78, 108685.

Ben Hamou, A., Escudero-Curiel, S., Iberache, N., Torres-Pinto, A., Jada, A., Pazos, M., El Alem, N. & Sanromán, Á. (2025) 'Peroxymonosulfate activation by iron-rich biochar derived from sewage sludge digestate for sulfamethoxazole degradation: A rigorous examination of performance and mechanistic insights', *Journal of Environmental Chemical Engineering,* 13, 119039.

Çako, E., Gunasekaran, K. D., Rajendran, S. & Zielińska-Jurek, A. (2024) 'Recent advances on magnetic carbon-related materials in advanced oxidation processes of emerging pollutants degradation', *Water Resources and Industry,* 31, 100241.

Cao, J., Jiang, Y., Tan, X., Li, L., Cao, S., Dou, J., Chen, R., Hu, X., Qiu, Z., Li, M., Chen, Z. & Zhu, H. (2024) 'Sludge-based biochar preparation: pyrolysis and co-pyrolysis methods, improvements, and environmental applications', *Fuel,* 373, 132265.

Chen, H., Long, Q., Zhang, Y., Yang, H. & Shu, J. (2024) 'Using red mud to prepare the iron-bearing catalyst for the efficient degradation of phenol in the Fenton-like process', *Arabian Journal of Chemistry,* 17, 105797.

Chen, H., Lu, N., Long, Q., Yang, M., Luo, D. & Wang, Z. (2026) 'Cobalt-doped red mud composite as a porous catalyst for activating peroxymonosulfate to degrade methylene blue', *Environmental Research,* 293, 123793.

Cui, K., Liu, H., Cao, X., Wu, P., Wang, J., Liu, X. & Qiu, J. (2025) 'Stepwise approach to environmental remediation: Effective Cu2+ adsorption and catalytic degradation of tetracycline using red mud and coal gasification slag-based magnetic zeolite LTA', *Chemical Engineering Journal,* 519, 164962.

Cui, W., Cui, Q., Dong, X., Liu, J., Song, K., Xie, M. & Yao, X. (2024) 'Current research status and emerging trends in utilization of red mud resources: A study based on bibliometric network analysis', *Construction and Building Materials,* 442, 137605.

Dai, Z., Liang, B., Chen, L., Zhang, W., Gao, Y. & Li, L. (2025) 'Rational construction of S-scheme ZnIn2S4/g-C3N4 heterojunction for effective sacrificial agent-free uranium photocatalysis in air', *Separation and Purification Technology,* 354, 129241.

Feng, Y., Wu, D., Liao, C., Deng, Y., Zhang, T. & Shih, K. (2016) 'Red mud powders as low-cost and efficient catalysts for persulfate activation: Pathways and reusability of mineralizing sulfadiazine', *Separation and Purification Technology,* 167, 136–45.

Fu, J., Li, H., Jiang, G., Feng, D., Yi, J., Liu, Y., Gong, R., Guo, J., Liu, P. & Cui, K. (2024) 'Enhanced removal of tetracycline hydrochloride by activation of persulfate with sludge-red mud magnetic biochar: Synergistic effect between adsorption and radical-nonradical pathways', *Inorganic Chemistry Communications,* 170, 113451.

Gao, L., Guo, Y., Zhan, J., Yu, G. & Wang, Y. (2022) 'Assessment of the validity of the quenching method for evaluating the role of reactive

species in pollutant abatement during the persulfate-based process', *Water Research,* 221, 118730.

Gu, J., Wei, G., He, Y., Zhang, Y., Xiong, D., Zhang, L., Zhou, Y. & He, S. (2024) 'Red mud-based Fe2O3/Cu-Al LDH prepared through mechanochemical synthesis as effective peroxymonosulfate activator for lomefloxacin hydrochloride degradation via radical-nonradical cooperation mechanisms', *Journal of Water Process Engineering,* 68, 106517.

Gu, J., Zhang, L., Ji, Y., Xue, R., Duan, G., Wei, G. & Li, B. (2025) 'Novel red mud-based FeS2 composite used as an effective heterogeneous catalyst for the degradation of levofloxacin: Preparation, application and degradation mechanism', *Materials Research Bulletin,* 182, 113143.

Hong, Y., Liu, Y., Xu, Q. & Lin, Z. (2026) 'Anchoring of carbon-coated iron nanoparticles with biochars enabled efficient peroxymonosulfate activation for degradation of tetracycline', *Inorganic Chemistry Communications,* 190, 116886.

Jian, C., Chen, P., Cheng, Z., Liu, L., Yan, C. & Qiu, F. (2025) 'Hydrogenated red mud biochar as visible-light-driven peroxymonosulfate (PMS) activators for efficient degradation of antibiotic: Resource utilization, mechanism insights and toxicity assessment', *Environmental Research,* 273, 121233.

Li, Q., Wei, G., Duan, G., Zhang, L., Li, Z. & Yan, F. (2022) 'Valorization of ball-milled waste red mud into heterogeneous catalyst as effective peroxymonosulfate activator for tetracycline hydrochloride degradation', *Journal of Environmental Management,* 324, 116301.

Li, Y., Zhang, C., Zhao, G., Su, P., Wang, J., Li, Y., Zhou, W., Mu, Y., Zhang, J. & Liu, W. (2024) 'A critical review on antibiotics removal by persulfate-based oxidation: Activation methods, catalysts, oxidative species, and degradation routes', *Process Safety and Environmental Protection,* 187, 622–43.

Liu, S., Wang, J., Liu, Y., Yang, B., Hong, M., Yu, S. & Qiu, G. (2024) 'Nickel-doped red mud-based Prussian blue analogues heterogeneous activation of H2O2 for ciprofloxacin degradation: waste control by waste', *Environmental Science and Pollution Research,* 31, 39439–53.

Liu, S., Wang, J., Liu, Y., Yang, B., Zhao, C., Yu, S., Wang, C., Qiu, G., Liu, J. & Fang, Y. (2025) 'Magnetic-supported catalyst derived from red mud-based Fe-Co PBA for efficient degradation of organic pollutants by activating peroxymonosulfate under visible light', *Separation and Purification Technology,* 354, 128954.

Medha, I., Chandra, S., Chauhan, S., Taksal, P. A., Tiwari, C. S., Mubarak, N. M., Bevara, S. & Kumar, A. (2025) 'Distribution of antibiotics in water resources and the role of biochar in advanced water treatment techniques for antibiotics removal in the quest for cleaner water', *Separation and Purification Technology,* 377, 134194.

Mohd Hanafiah, Z., Wan Mohtar, W. H. M., Rohani, R., Fadzizi, M. F., Wan-Mohtar, W. a. a.-Q. I., Sayed, K., Manan, T. S. B. A. & Indarto, A. (2024) 'Removal of pharmaceutical compounds from sewage effluent by the nanofiltration membrane', *Journal of Water Process Engineering,* 68, 106320.

Pattnaik, A., Patra, A. R., Barman, P. A., Poonia, A. K. & Ghosh, P. (2025) 'An overview of activation strategies in persulfate advanced oxidation processes: Current and critical perspectives on pathways for organic pollutant remediation', *Journal of Environmental Chemical Engineering,* 13, 120269.

Qin, D., Rong, H., Guo, D., Nkinahamira, F., Wang, J., Luo, J., Tian, T. & Wu, H. (2025) 'Red mud-based materials for mitigating antibiotic pollution in wastewater: a critical review of adsorption and advanced oxidation processes', *Separation and Purification Technology,* 379, 134984.

Qiu, J., Yang, J.-L., Cui, K.-B., Cao, X.-J., Lyu, J.-W., Liu, H.-Z., Wang, J.-Z., Wang, G.-F. & Liu, X. (2025) 'Synergistic waste valorization: One-step hydrothermal synthesis of magnetic hydrochar from red mud and peanut shells for effective methylene blue adsorption', *Materials Chemistry and Physics,* 342, 130994.

Sayed, K., Wan-Mohtar, W. H. M., Mohd Hanafiah, Z., Bithi, A. S., Md Isa, N. & Abd Manan, T. S. B. (2024a) 'Occurrence of pharmaceuticals in rice (Oryza sativa L.) plant through wastewater irrigation', *Environmental Toxicology and Pharmacology,* 109, 104475.

Sayed, K., Wan Mohtar, W. H. M., Hanafiah, Z. M., Wan-Mohtar, W. a. a. Q. I., Abd Manan, T. S. B. & Mohamad Sharif, S. a. B. (2024b) 'Simultaneous enhanced removal of pharmaceuticals and hormone from wastewaters using series combinations of ultra-violet irradiation, bioremediation, and adsorption technologies', *Journal of Water Process Engineering,* 57, 104589.

Sayed, K., Wan Mohtar, W. H. M., Mohd Hanafiah, Z., Md Isa, N., Yi Jie, C. E. & Syakir, M. I. (2025) 'Uptake of Pharmaceuticals in Rice Plant Cultivars Through Reclaimed Water Irrigation: Impact on Food Security', *Exposure and Health,* 17, 1241–67.

Sayed, K., Wan Mohtar, W. H. M., Mohd Hanafiah, Z., Sultana Bithi, A. & Wan-Mohtar, W. a. a. Q. I. (2024c) 'Removal Of Pharmaceuticals from Municipal Wastewater Using Malaysian Ganoderma Lucidum Fungal Strain', *Jurnal Kejuruteraan*.

Shen, C., Dong, X., Yang, J., Li, Y., Cui, S., Zhang, D. & Lin, X. (2025) 'Red mud-based magnetic biochar composite as a peroxydisulfate activator for tetracycline degradation', *Environmental Research,* 279, 121793.

Shi, Q., Yang, R., Liu, M., Feng, Y., Li, Z. & Zhu, W. (2024) 'A highly-efficient peroxymonosulfate activator using a sewage sludge derived biochar supported cobalt oxide: Mechanism and characteristics', *Process Safety and Environmental Protection,* 192, 1319–29.

Stapleton, M. J., Ansari, A. J. & Hai, F. I. (2023) 'Antibiotic sorption onto microplastics in water: A critical review of the factors, mechanisms and implications', *Water Research,* 233, 119790.

Thi Mai, N., Van Thanh, D., Nhat Huy, N., Danh Bich, D., Thi Minh Hang, T., Huu Hao, N. & Manh Khai, N. (2025) 'Red mud supported on rice husk biochar as sono-photo-Fenton catalysts for degradation of ciprofloxacin in water', *Separation and Purification Technology,* 354, 129039.

Tian, Z., Wan, H., Jin, R., Qiu, X., Bamanu, B. & Zhao, Y. (2025) 'Regulating the surface structure of sludge biochar by mixed-acid washing to enhance the activation of peroxymonosulfate for sulfamethoxazole removal', *Journal of Water Process Engineering,* 71, 107123.

Wang, Y., Fang, W., Cheng, M., Li, W., Cen, Q., Li, B. & Liu, Z. (2025) 'A review on the application of iron-carbon composites prepared from red mud and organic solid waste for wastewater treatment', *Desalination,* 614, 119202.

Xiao, J., Zhang, L., Gu, J., Li, B., Yuan, Y., Wei, G. & Li, P. (2025) 'Enhanced degradation of high concentration lomefloxacin hydrochloride by three-dimensional electrocatalytic system with novel red mud-based CuFeS2/FeS2 particle electrode', *Separation and Purification Technology,* 360, 131214.

Xu, B., An, Q., Deng, S., Li, Z., Yang, Z., Wu, H. & Ye, Z. (2023a) 'Acid-modified red mud biochar for the degradation of tetracycline: Synergistic effect of adsorption and nonradical activation', *Journal of Environmental Management,* 347, 119077.

Xu, K., Lin, Q., Fan, X., Zheng, J., Liu, Y., Ma, Y. & He, J. (2023b) 'Enhanced degradation of sulfamethoxazole by activation of peroxodisulfate with red mud modified biochar: Synergistic effect between adsorption and nonradical activation', *Chemical Engineering Journal,* 460, 141578.

Xu, X., Dong, H., Liu, J., Zhuang, J., Huang, T., Gan, Y. & Wu, B. (2025) 'Phosphate-ligand engineered biochar with electron-donor and nanoconfinement effects for selective antibiotic adsorption', *Chemical Engineering Journal,* 522, 167713.

Yang, M., Zhao, X., Wang, X., Rui, H., Wang, L., Han, C., Zheng, B., Guo, B. & Xie, H. (2026) 'Effect of pyrolysis atmosphere on iron-based biochar for activated peroxymonosulfate and sulfamethoxazole removal: A comparison of microstructure and performance', *Colloids and Surfaces A: Physicochemical and Engineering Aspects,* 744, 140596.

Yang, Z., An, Q., Deng, S., Xu, B., Li, Z., Deng, S., Zhao, B. & Ye, Z. (2023) 'Efficient activation of peroxydisulfate by modified red mud biochar derived from waste corn straw for levofloxacin degradation: Efficiencies and mechanisms', *Journal of Environmental Chemical Engineering,* 11, 111609.

Zeng, Q., Xu, Z., Liang, D., Liu, Y., Huang, J., Xie, W. & Liu, J. (2025) 'Red mud modified biochar for peracetic acid activation to degrade sulfamethazine: A non-radical-dominated mechanism', *Environmental Research,* 285, 122627.

Zhang, W., Li, M., Lin, L., Li, M. & Sun, F. (2024) 'Peroxyacetic acid activation by cobalt-doped peanut shell biochar for efficient CBZ degradation: Role of organic radicals, singlet oxygen, and high-valent cobalt species', *Separation and Purification Technology,* 330, 125592.

Zhang, X., Zhang, Y., Zhang, S., Yao, L. & Hao, Y. (2025) 'Lignocellulosic biomass pyrolysis: A review on the pretreatment and catalysts', *Fuel Processing Technology,* 279, 108352.

Zhao, H., Ji, Y., Kong, D., Lu, J., Yin, X. & Zhou, Q. (2019) 'Degradation of iohexol by Co2+ activated peroxymonosulfate oxidation: Kinetics, reaction pathways, and formation of iodinated byproducts', *Chemical Engineering Journal,* 373, 1348–56.